fire

MDPI

Article

Numerical Study on the Combustion and Emissions Characteristics of Liquid Ammonia Spray Ignited by Dimethyl Ether Spray

Yupeng Leng [1,2], Liming Dai [3,*], Qian Wang [3], Jiayu Lu [3], Ouqing Yu [3] and Nigel John Simms [2]

[1] Institute for Energy Research, Jiangsu University, Zhenjiang 212013, China
[2] School of Water, Energy and Environment, Cranfield University, Cranfield MK43 0AL, UK
[3] School of Energy and Power Engineering, Jiangsu University, Zhenjiang 212013, China
* Correspondence: liming_dai@ujs.edu.cn

Abstract: Ammonia has attracted considerable attention as a zero-carbon fuel for decarbonizing energy-intensive industries. However, its low reactivity and narrow flammability limit efficient ignition and efficient combustion. By using CONVERGR software, this study numerically investigates the ignition and combustion characteristics of liquid ammonia spray ignited by dimethyl ether spray in a constant-volume chamber at an ambient temperature of 900 K. Critical parameters, including injection angles (90°–150°), liquid ammonia injection pressures (60–90 MPa), and ambient pressures (2.8–5.8 MPa), were systematically analyzed to evaluate their effects on ignition conditions and emissions. Results indicate that increasing the injection angle improves mixing between liquid ammonia and dimethyl ether sprays, enhancing combustion efficiency and achieving a maximum efficiency of 92.47% at 120°. Excessively large angles cause incomplete combustion or misfire. Higher liquid ammonia injection pressures improve atomization and promote earlier interactions between the sprays but reduce combustion efficiency, decreasing by approximately 2% as injection pressure increases from 60 MPa to 90 MPa. Higher ambient pressures improve combustion stability but decrease ammonia combustion efficiency. Post-combustion NO emissions at 5.8 MPa are reduced by 60.48% compared to 3.8 MPa. The formation of NO is strongly correlated with the combustion efficiency of liquid ammonia. A higher combustion rate of liquid ammonia tends to result in elevated NO. Based on these findings, an injection angle of 120°, an NH_3 injection pressure of 75 MPa, and an ambient pressure of 3.8 MPa are recommended to optimize combustion efficiency.

Keywords: ammonia; dimethyl ether; high-pressure direct injection; ammonia ignition enhancement

check for updates

Academic Editor: Jiaqiang E

Received: 30 November 2024
Revised: 24 December 2024
Accepted: 29 December 2024
Published: 31 December 2024

Citation: Leng, Y.; Dai, L.; Wang, Q.; Lu, J.; Yu, O.; Simms, N.J. Numerical Study on the Combustion and Emissions Characteristics of Liquid Ammonia Spray Ignited by Dimethyl Ether Spray. *Fire* **2025**, *8*, 14. https://doi.org/10.3390/fire8010014

Copyright: © 2024 by the authors. Licensee MDPI, Basel, Switzerland. This article is an open access article distributed under the terms and conditions of the Creative Commons Attribution (CC BY) license (https://creativecommons.org/licenses/by/4.0/).

1. Introduction

Traditional fossil fuel combustion has long served as a primary energy source for human society [1]. However, it generates significant challenges, including greenhouse gas emissions and soot formation. Greenhouse gas emissions have contributed significantly to global warming, leading to severe environmental damage [2]. Zero-carbon fuels have emerged as a promising solution to mitigating greenhouse gas emissions [3]. Among them, hydrogen and ammonia exhibit great potential, as they primarily produce nitrogen and water as byproducts [4–6]. The high reactivity and wide flammability range of hydrogen make it prone to explosions. Furthermore, the high costs of hydrogen liquefaction, storage, and transportation have limited its widespread adoption [7]. Ammonia, synthesized using

renewable energy sources like solar and wind power, can achieve carbon neutrality over its lifecycle [8]. Ammonia can be stored in liquid phase at 1 MPa, offering low-cost storage and transportation benefits [9–11]. However, ammonia fuel faces several limitations, such as low calorific value, a slow combustion rate, and an ignition temperature approximately 400 K higher than that of diesel [12], all of which significantly affect its combustion stability [13,14]. A compression ratio of at least 35:1 is required for the compression ignition engine, highlighting the stringent requirements for pure ammonia combustion [4]. Therefore, highly reactive fuels, such as diesel [15], biodiesel [16], hydrogen [17], and dimethyl ether (DME) [18,19], are blended with ammonia to improve ignition and enhance combustion stability. Liu et al. [20] investigated ammonia/diesel dual-fuel stratified injection modes in marine engines, achieving power output comparable to that of conventional diesel engines with NO_x emissions of lower than 3.4 g/kW·h. Elumalai et al. [21] demonstrated that igniting ammonia with biodiesel at a 44% substitution rate resulted in reductions of 44%, 32%, 48%, 55%, and 66% for HC, CO, CO_2, NO_x, and soot emissions, respectively.

Previous studies on ammonia combustion engines primarily investigated port injection of gaseous ammonia, where it mixes with air in the intake manifold before entering the cylinder for combustion [22]. Xu et al. [23] examined ammonia port injection combined with diesel direct injection and observed that the low propagation speed of the premixed flame led to substantial unburned ammonia, achieving only 53% combustion efficiency. Yousefi et al. [24] observed that unburned ammonia tends to accumulate in crevices and boundary layers during premixed combustion. To mitigate this issue, high-pressure direct injection (HPDI) of ammonia has emerged as a key strategy to enhance engine performance. Li et al. [25] reported that high-pressure direct injection of fuels increased the ammonia substitution rate by 17% compared to low-pressure direct injection while reducing unburned ammonia, NO_x, and greenhouse gas emissions. Liu et al. [26] reported that raising the diesel injection pressure from 80 Mpa to 120 Mpa resulted in a higher peak in-cylinder pressure and improved combustion efficiency to 82.64% in the ammonia/diesel dual-fuel engine. Zhou et al. [27] made a comparison between the high-pressure direct injection of fuel and the low-pressure direct injection strategy in a marine engine, which shown that high-pressure direct injection results in a lower indicated thermal efficiency but 47% NO_x emissions compared to the original engine. Shi et al. [28] investigated the combustion and pollutant performance at a 40% ammonia energy fraction using collaborative optimization of fuel injection timing and angle. This approach achieved just 0.28 g/kW·h unburned ammonia emissions and a 34% reduction in greenhouse gas emissions.

Unlike diesel or biodiesel, DME lacks C-C bonds, resulting in nearly zero soot emissions during combustion [29]. It can also be produced through renewable methods, such as biogas gasification [30] and waste treatment [31]. Additionally, the high cetane number of DME improves combustion efficiency and stability [32], making it as an excellent ignition agent for ammonia combustion. Gross et al. [33] investigated premixed liquid ammonia/DME fuel in compression ignition engines and found that higher ammonia ratios extended ignition delay and elevated CO, HC, and NO_x emissions while maintaining exceptionally low soot emissions. Ryu et al. [34] proposed that a fuel mixture comprising 40% DME and 60% NH_3 energy fractions provides stable combustion characteristics. Studies on DME/NH_3 dual-fuel combustion have primarily focused on premixed combustion. However, premixed NH_3/DME fuels lack flexible control over ignition timing and combustion phases. Specifically, the fuel ratio must be adjusted rapidly to accommodate fluctuations in engine load. As we know, no studies have yet investigated NH_3 spray directly ignited by DME spray, emphasizing the need to explore ignition, combustion, and emissions mechanisms in such systems.

2. Numerical Methodologies

2.1. Model Establishment

This study investigates the detailed ignition process of liquid ammonia spray ignited by a DME spray. The high reactivity of DME facilitates rapid auto-ignition over a broad range of operating conditions. Furthermore, the flexible nozzle arrangement and injection conditions enable dynamic optimization of ignition and combustion phase control. Three-dimensional numerical simulations were performed using computational fluid dynamics (CFD) software Converge to assess the effects of various operating parameters, including injection angles, NH_3 injection pressures, and ambient pressures, on ignition characteristics, combustion efficiency, and emissions. The findings provide valuable insights into the direct ignition of NH_3 by DME, as well as the design and development of NH_3/DME dual-fuel engines. They also offer guidance for optimizing injection strategies to improve combustion efficiency and reduce emissions.

Numerical simulations were conducted in a constant-volume chamber, as depicted in Figure 1a. The constant-volume chamber dimensions were set to 100 mm × 100 mm × 100 mm. The simulations employed validated spray models for both liquid ammonia and DME, each delivered through a dedicated injector. The injectors were symmetrically arranged, positioned opposite each other, and equipped with a single nozzle per injector. Spray patterns were defined by injector orientation and specific nozzle configurations. A cross-sectional diagram of the spray jets is shown in Figure 1b, with the blue region indicating the DME spray and the red region representing the liquid ammonia spray. The simulation starts at 0 ms, with both fuels injected into the chamber simultaneously, and concludes at 6 ms. The nozzle configuration plays a crucial role in determining the spray morphology, which directly impacts combustion characteristics, including stability, efficiency, and emissions formation. The nozzle injection angle critically governs spray direction and distribution, influencing fuel–air mixing, ignition behavior, and combustion efficiency. Additionally, this study examines the effects of injection and ambient pressures on ignition characteristics and emissions profiles. The properties of DME and ammonia are listed in Table 1, while Table 2 provides the simulation conditions, including chamber size, ambient temperature, injector spacing, nozzle diameters, and other key parameters. DME is significantly more reactive than liquid ammonia, with a higher propensity for auto-ignition at 900 K. This high reactivity enables DME to ignite the ammonia spray upon contact subsequently. The simulations examine nozzle angles (90°, 105°, 120°, 135°, and 150°) and injection pressures for ammonia (60, 75, and 90 MPa) and DME (75 MPa). Ambient pressures (2.8, 3.8, 4.8, and 5.8 MPa) were varied to evaluate their effects on ignition and emissions performance.

Table 1. Comparison of properties between liquid ammonia and DME.

Parameter	Ammonia	DME
Boiling point/K	239.8	358
Autoignition temperature/K	924	623
Octane number	130	55
Lower heating value/(MJ/kg)	18.8	28.43
Latent heat of vaporization/(KJ/kg)	1.37	460
Laminar burning velocity/(m/s)	0.07	0.54

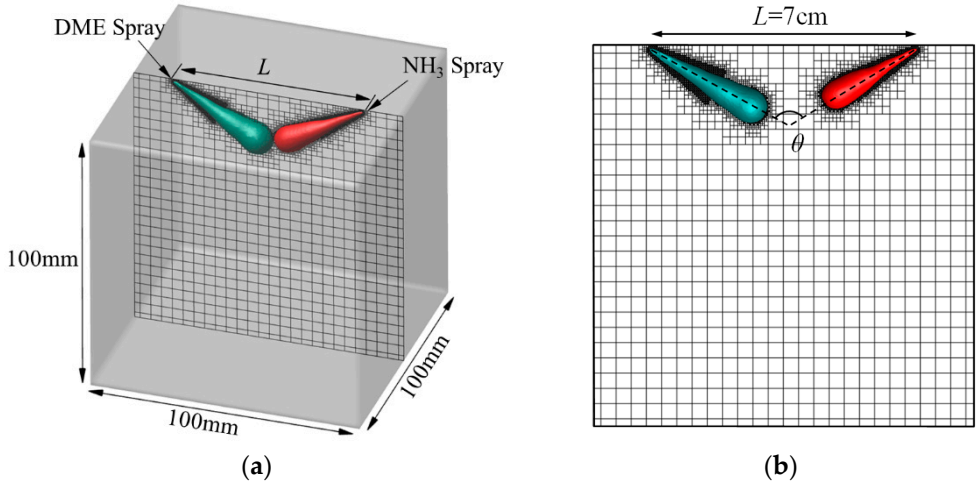

Figure 1. Schematic diagram of the model. (**a**) Geometric structure, (**b**) Cross-sectional visualization of fuel spray.

Table 2. Chamber specifications and operation parameters.

Parameter	Value
Chamber size/mm	100 × 100 × 100
Ambient temperature/K	900
Ambient gas	Air
Injector distance/cm	7.0
DME injection pressure/MPa	75
Ammonia nozzle diameter/mm	0.22
DME nozzle diameter/mm	0.18
Ammonia injection mass/mg	18.15
DME injection mass/mg	3
Nozzle angle/°	90, 105, 120, 135, 150
NH_3 injection pressure/MPa	60, 75, 90
Ambient pressure/MPa	2.8, 3.8, 4.8, 5.8

A small quantity of DME is used to ignite the liquid ammonia spray, achieving an ammonia substitution ratio (ASR) [35] of 80%. The ASR, which represents the energy contribution of liquid ammonia relative to the total energy of the dual fuels, is defined as:

$$ASR = \frac{m_{NH_3} \cdot LHV_{NH_3}}{m_{NH_3} \cdot LHV_{NH_3} + m_{DME} \cdot LHV_{DME}} \cdot 100\% \quad (1)$$

where m_{NH_3} and m_{DME} represents the injection masses of NH_3 and DME, respectively. LHV_{NH_3} and LHV_{DME} denote their lower heating values, specified as 18.8 MJ/kg for NH_3 and 28.43 MJ/kg for DME.

In this study, the combustion efficiency of ammonia is calculated using the ratio of the mass of ammonia that has been successfully combusted to the total mass of ammonia injected into the system. The NH_3 combustion efficiency (η_{NH_3}) can be expressed as:

$$\eta_{NH_3} = \frac{m_{combusted}}{m_{injected}} \quad (2)$$

where $m_{combusted}$ is the mass of ammonia that undergoes complete combustion, producing nitrogen (N_2) and water vapor (H_2O), and $m_{injected}$ is the total mass of ammonia injected into the combustion chamber.

2.2. Model Verification and Operation

The ignition of liquid ammonia spray by DME spray involves complex physical processes and chemical reactions, with simulation results strongly dependent on the selection of physicochemical models. The Kelvin–Helmholtz and Rayleigh–Taylor (KH-RT) model [36] was applied to simulate droplet breakup and atomization. The KH (Kelvin–Helmholtz) model primarily simulates primary and secondary droplet breakup caused by the instability of cylindrical jets and liquid viscosity. In the KH model, the breakup time (τ_{KH}) and the droplet radius after breakup (r_{KH}) are defined as follows:

$$\tau_{KH} = \frac{3.726 B_1 r_0}{\Lambda_{KH} \Omega_{KH}},\ r_{KH} = B_0 \Lambda_{KH} \quad (3)$$

where r_0 represents the initial droplet radius, Λ_{KH} is the wavelength of the perturbation wave, and Ω_{KH} means the maximum growth rate of the perturbation wave.

The RT (Rayleigh–Taylor) model simulates droplet breakup caused by drag forces, suggesting that RT wave instability induces liquid breakup at a specific distance from the nozzle. The breakup time (τ_{RT}) and droplet radius after breakup (r_{RT}) are expressed as:

$$\tau_{RT} = \frac{C_\tau}{\Omega_{RT}},\ r_{RT} = \frac{C_{RT} \Lambda_{RT}}{\Omega_{RT}} \quad (4)$$

where Λ_{RT} denotes the wavelength of the most unstable perturbation wave and Ω_{RT} represents its frequency.

Due to significant differences in physical properties such as viscosity and density, liquid ammonia (NH_3) and DME require distinct parameter settings in the KH–RT spray breakup models. Table 3 details the parameter settings for the KH–RT models of DME and NH_3.

Table 3. Parameter settings for DME and liquid ammonia KH–RT models.

Parameter	Value
B_1 of DME	11
B_1 of NH_3	8
B_0	0.61
C_τ	1
C_{RT}	0.1

In addition to the KH–RT model, the Redlich–Kwong equation [37] was employed to characterize gas states, while the RNG k-ε [38] was utilized to capture turbulence effects. Droplet collisions and wall interactions were modeled using the method proposed by O'Rourke and Amsden [39]. The No Time Counter (NTC) method and Frossling correlation [40] were used to simulate droplet collisions and evaporation, respectively. The Frossling correlation model was used to characterize the drop evaporation model. The SAGE model [41] simulates fuel ignition and combustion by accounting for temperature and species concentrations in each computational cell. Also, the extended Zeldovich model [41] is used to predict the NO_x emissions in the combustion process. This study employs the NH_3/DME dual-fuel mechanism developed by Xiao et al. [14], which includes 102 species and 594 chemical reactions, demonstrating reliable predictions of laminar burning velocity and ignition delay under diverse operating conditions.

The accuracy of the spray characteristics of the fuels significantly impacts the precision of the simulation results [42]. Independent spray models were validated for both liquid ammonia and DME to ensure accuracy. Liquid ammonia spray validation was performed using constant-volume chamber experiments conducted by Li et al. [25]. The initial and boundary conditions in the simulation were aligned with those of the experiment, as

detailed in Table 4. The computational domain was defined as a rectangular box with dimensions of 48 mm × 48 mm × 97 mm. A grid independence study was conducted to determine the optimal mesh size for the model. Base grid sizes of 2 mm, 4 mm, 6 mm, and 8 mm were evaluated. In the spray development region, four levels fixed grid refinement were applied, incorporating four levels of adaptive mesh refinement (AMR) driven by velocity and temperature gradients. As shown in Figure 2, the validation results demonstrate high accuracy with base grid sizes of 2 mm and 4 mm, whereas significant overestimations in vapor–liquid penetration distance were observed with 6 mm and 8 mm grids. Therefore, a 4 mm base grid size was selected to balance computational efficiency and simulation accuracy. As injection time increased, the vapor-phase penetration distance of the liquid ammonia spray continued to grow, whereas the liquid-phase penetration distance initially rose but stabilized after approximately 0.5 ms, remaining constant thereafter. Figure 3 compares the simulated results with the simulation and experimental spray morphologies from Li et al. [25], where solid red lines represent liquid-phase ammonia spray and dashed red lines denote gas-phase ammonia spray. The results confirm that the spray model accurately predicted the liquid ammonia spray morphology, validating its applicability for numerical simulations in this study.

Table 4. Validation conditions for liquid ammonia spray.

Parameter	Value
Nozzle diameter/mm	0.22
Injection pressure/MPa	60
Fuel temperature/K	350
Ambient temperature/K	900
Ambient gas	N_2
Ambient density/(kg·m^{-3})	18.0

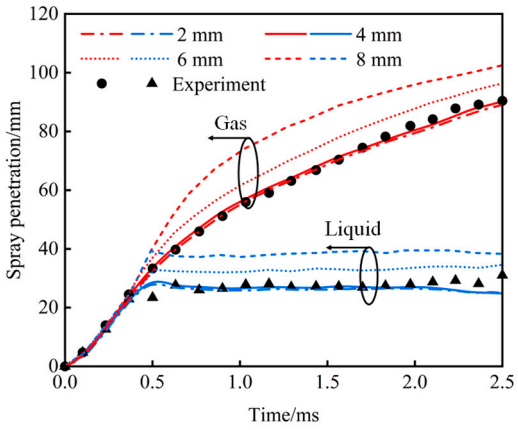

Figure 2. Grid independent validation for liquid ammonia spray penetrations.

The DME spray injection model is based on spray experiments conducted by Cung et al. [43] in a constant-volume chamber under inert and oxygen-enriched conditions. Validation conditions for the DME spray are detailed in Table 5. To ensure consistency across simulations, the DME spray validation employs the same grid size, refinement levels, and turbulence model parameters as those used for liquid ammonia. The simulated and experimental results for DME vapor-phase and liquid-phase penetration distances are compared in Figure 4. While the simulated liquid-phase penetration distance slightly exceeded the experimental results during the later stages of the spray, the results overall align well. Simulated and experimental values for ignition delay time (ID) and flame lift-off length (LOL) under varying ambient densities, temperatures, and oxygen concentrations

are compared in Figure 5. Ignition delay time (ID) is defined as the interval from the start of injection to the point of the maximum temperature gradient, while lift-off length (LOL) represents the minimum axial distance where the Favre-averaged OH mass fraction reaches 14% of its peak value [44]. The simulated and experimental data exhibited strong agreement for ignition delay time and lift-off length under high oxygen concentrations. However, the slight deviations in simulated LOL values at low oxygen concentrations are primarily attributed to limitations in the chemical reaction kinetics model. Since this study focuses on high-oxygen concentration conditions, the DME spray model was validated to ensure high accuracy under both combustion and non-combustion scenarios.

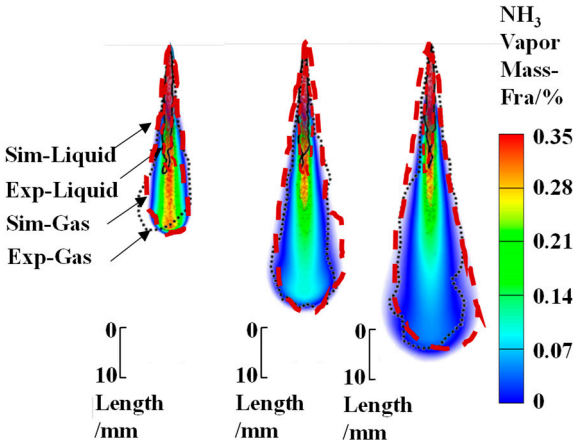

Figure 3. Comparison between simulation and experiment of NH_3 spray.

Table 5. Validation conditions for DME spray.

Parameter	Value
Nozzle diameter/mm	0.18
Injection pressure/MPa	75
Fuel temperature/K	383
Ambient temperature/K	900, 1100
Ambient density/(kg·m^{-3})	14.8, 25.0, 30.0
Oxygen concentration/%	0, 15, 18, 21

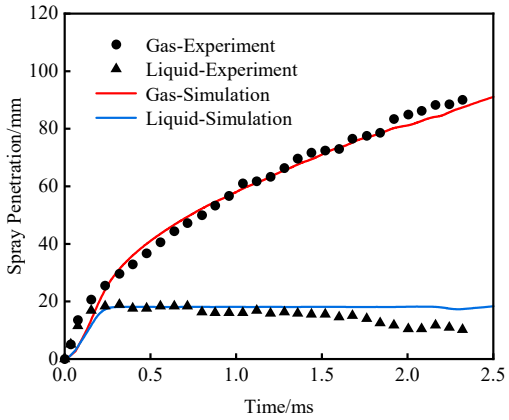

Figure 4. Validation of DME spray penetration under non-combustion condition.

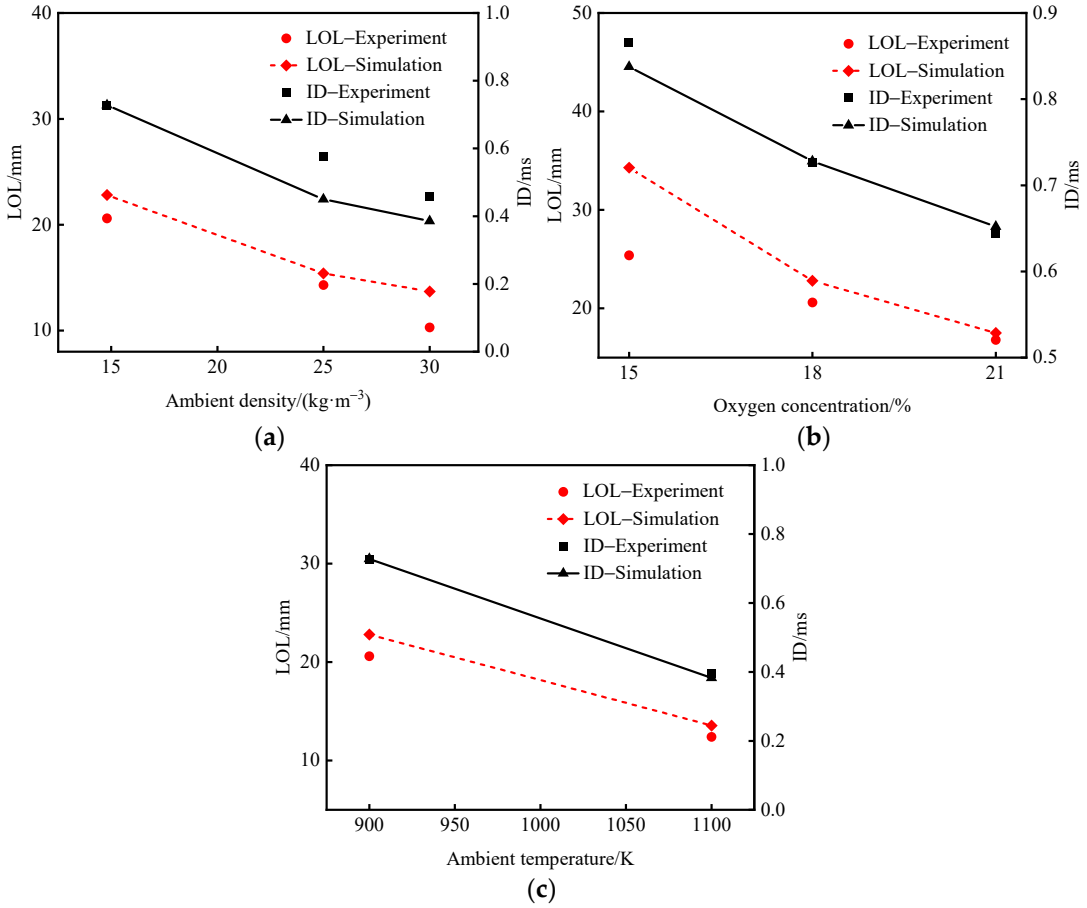

Figure 5. Validation of ignition delay times and flame lift-off lengths. (**a**) Effect of ambient density; (**b**) Effect of oxygen concentration; (**c**) Effect of ambient temperature.

3. Results and Discussion

3.1. Effect of Injection Angle on Ignition and Combustion Process

The injection angle plays a critical role in the ignition process. This study investigates the impact of varying θ from 90° to 150°, as detailed in Table 2. The maximum temperature corresponding to different injection angles is presented in Figure 6a. At large injection angles (135°–150°), ignition fails and the peak maximum temperature decreases significantly as θ increases. At θ = 150°, the maximum temperature gradually rises after 1.00 ms and stabilizes at approximately 1060 K by 4 ms. This is attributed to the large injection angle, which disperses the DME spray through interaction with the ammonia spray, leaving residual DME at the top of the chamber. The residual DME continuously evaporates, absorbing heat and undergoing a slow oxidation process, slightly increasing the local temperature. However, ignition fails due to the insufficient local fuel concentration. When θ < 135°, the DME spray successfully ignites the liquid ammonia spray. As θ decreases, the interaction between the DME and liquid ammonia sprays is delayed, enabling more complete combustion of the DME and a gradual rise in the maximum peak temperature. After 1.10 ms, the cooling effect of the liquid ammonia spray intensifies, causing a more rapid temperature decline. The liquid ammonia combustion efficiency, defined as the ratio of the mass of consumed NH_3 at the end of combustion to the total injected amount, at various θ is presented in Figure 6b. The results indicate that, under combustible modes, increasing θ gradually improves the combustion efficiency of liquid ammonia. At θ = 120°, liquid ammonia combustion reaches its maximum efficiency of 92.47%.

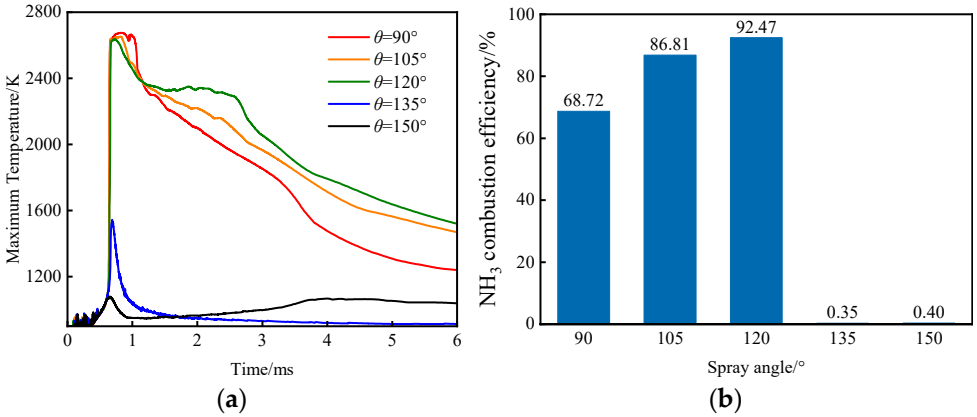

Figure 6. Thermal conditions for different θ. (**a**) Maximum temperature, (**b**) Liquid ammonia combustion efficiency.

The temperature distributions at ignition moments for various θ are shown in Figure 7, where black particles represent the spray dynamics of DME and ammonia. At θ = 90°, the DME ignites without interacting with the liquid ammonia spray. At θ = 105° and 120°, the DME spray successfully ignites the liquid ammonia spray upon interaction. The low density of the liquid ammonia spray at the leading edge results in insufficient heat absorption, which fails to extinguish the DME flame core. When θ range from 135° to 150°, the temperature at the front of the DME spray decreases, and the high-temperature region contracts. Evaporating droplets at the leading edge of the liquid ammonia spray absorb heat, hindering heat transfer at the interacting surface. The rapid evaporation and heat absorption of liquid ammonia suppress the DME's temperature rise, preventing sufficient reaction time and heat for combustion, ultimately causing misfire. The velocity contours of dual fuels interacting at the ignition moment are presented in Figure 8. The axial velocity of the liquid ammonia spray decreases gradually, whereas the radial velocity drops sharply, resulting in higher velocities at the center. Interaction with the DME spray and the relatively high velocity of the liquid ammonia spray create a velocity difference with the surrounding air, intensifying vortices and enhancing air entrainment. At θ = 150°, the excessively large angle reduces the vertical distance between the contact point and the wall, restricting vortices and altering their direction. Although increasing the nozzle angle improves fuel mixing, an excessively large angle increases the risk of spray impingement on the wall, exacerbating incomplete combustion and leading to misfire.

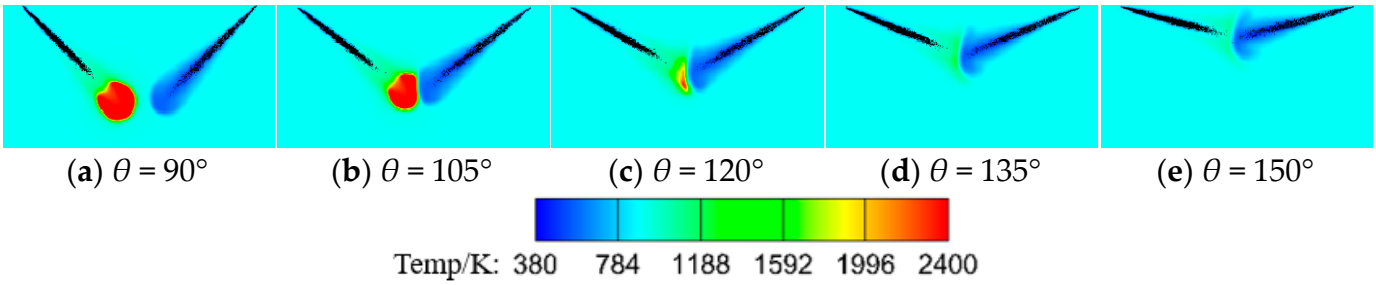

Figure 7. Temperature contours at ignition moment with different θ.

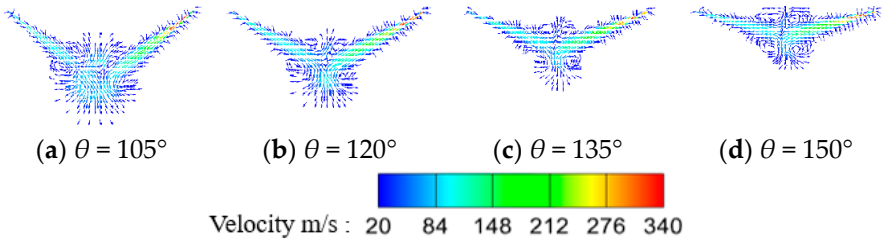

Figure 8. Velocity contours at ignition moment with different θ.

The distributions of temperature, OH, NH_3, DME, NH_2, NO, and NO_2 are depicted in Figures 9 and 10 for $\theta = 90°$. At 0.66 ms, DME ignition generates a high-temperature flame that initially does not interact with the liquid ammonia spray. The DME flame burns steadily and propagates until it contacts and ignites the ammonia spray at 0.90 ms. During the interaction, the ammonia spray front evaporates continuously, increasing its temperature and reducing penetration speed. However, at this stage, the flame front does not fully envelop the ammonia spray. By 2.50 ms, the DME is nearly consumed, allowing NH_3 to dominate the combustion process. The outer boundary of the OH radical distribution represents the flame front and highlights the flame propagation during combustion. Minimal OH radical presence indicates inefficient ammonia combustion, as shown in Figure 6b. OH radicals are predominantly generated during DME combustion and are less prominent during NH_3 combustion. By 3.00 ms, OH radicals nearly disappear, leaving a substantial amount of unburned NH_3, indicating low ammonia combustion efficiency. Huo et al. [45] defined the onset of NH_3 combustion by detecting NH_2 formation in their study of ammonia premixed combustion. Similarly, this study adopts NH_2 formation as an indicator of liquid ammonia combustion. NH_3 combustion begins at 0.90 ms, with NH_2 appearing in the center of the DME spray and at the front of the ammonia spray. As shown in Figure 10, ammonia combustion generates NO and NO_2, with NO predominantly concentrated in high-temperature regions, closely aligning with the OH distribution. The primary pathway for NO formation in ammonia flames involves the decomposition of ammonia into NH_i radicals, which are subsequently oxidized to HNO. This is evident from the alignment of NH_2 contours with the inner OH contours. NH_3 begins to decompose before the flame front reaches its peak temperature, resulting in NO formation near the flame front. At 0.90 ms, significant NO generation indicates an ammonia-rich combustible region. The mass fraction of NO_2 is lower than that of NO and primarily occurs in medium- to low-temperature regions, especially in the mid and rear sections of the DME spray. At high temperatures, NH_2 reacts with O_2 and O (Equations (5) and (6)) to form NO, while at lower temperatures, NO is reduced, as shown in Equation (7):

$$NH_2 + O_2 = NO + H_2O \quad (5)$$

$$NH_2 + O = NO + H_2 \quad (6)$$

$$NH_2 + NO = N_2 + H_2O \quad (7)$$

Figure 11 depicts the NO and NO_2 emissions across different θ. For all injection angles, NO emissions rise sharply after the ignition of NH_3, indicating rapid ammonia combustion and subsequent NO formation. As θ increases, the peak NO emissions rise significantly, with $\theta = 120°$ showing the highest peak, which is approximately 28.94% higher than that at $\theta = 90°$. This increase is attributed to enhanced atomization and mixing at larger injection angles, which improve combustion efficiency, promote more complete ammonia combustion, and elevate flame temperatures—intensifying NO formation pathways. By 6 ms, combustion enters the post-combustion phase, with NO emissions stabilizing. At

θ = 90°, NO emissions are approximately 55.63% of those at θ = 120°. NO_2 emissions remain consistently low and stable across all injection angles. Unlike NO, NO_2 formation is less sensitive to temperature, as it predominantly results from the reaction of NO with O_2 in lower-temperature post-flame regions. These findings highlight the importance of optimizing the injection angle to achieve high combustion efficiency while minimizing emissions. Therefore, a spray angle of 120° is selected for further studies.

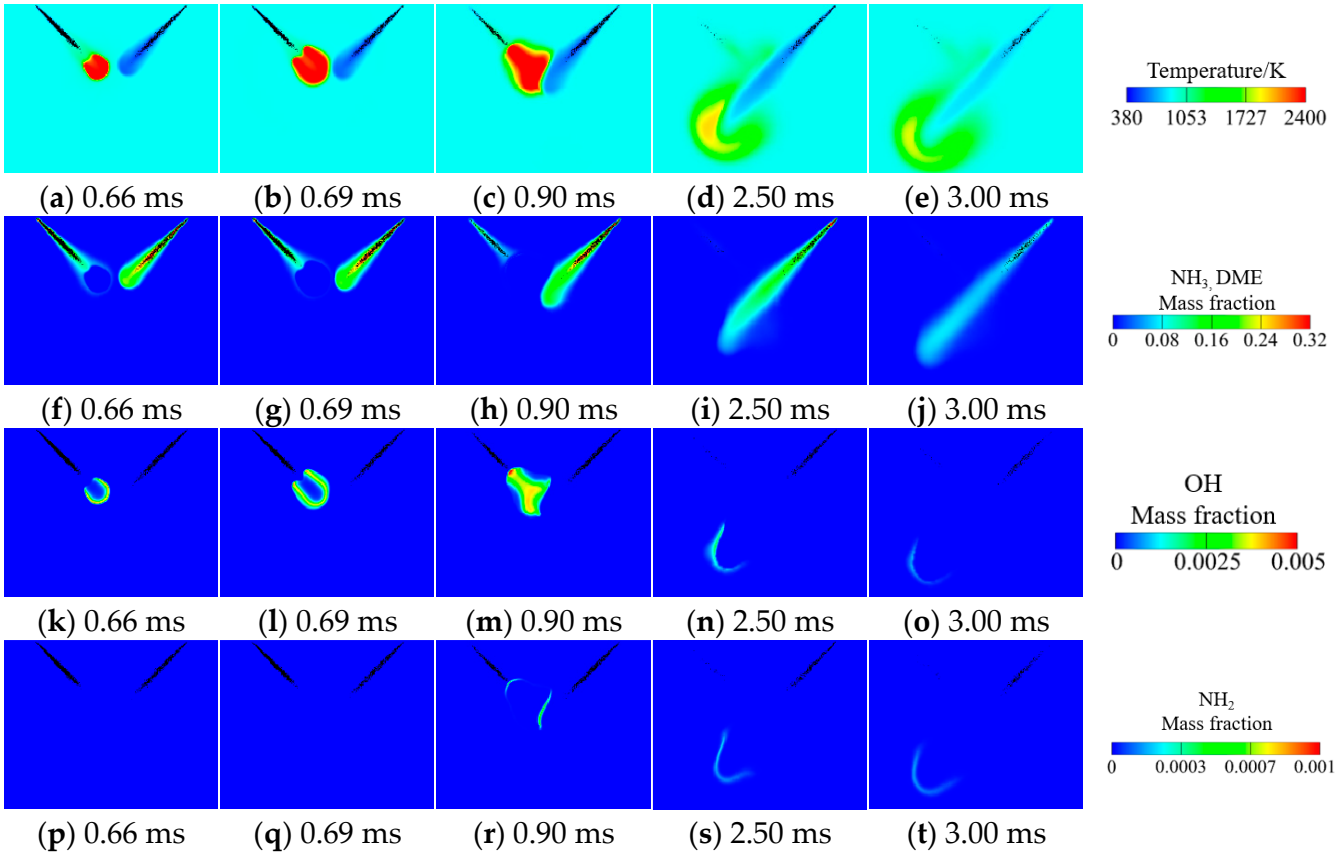

Figure 9. The temperature, OH, NH_3, DME, and NH_2 distributions at θ = 90°.

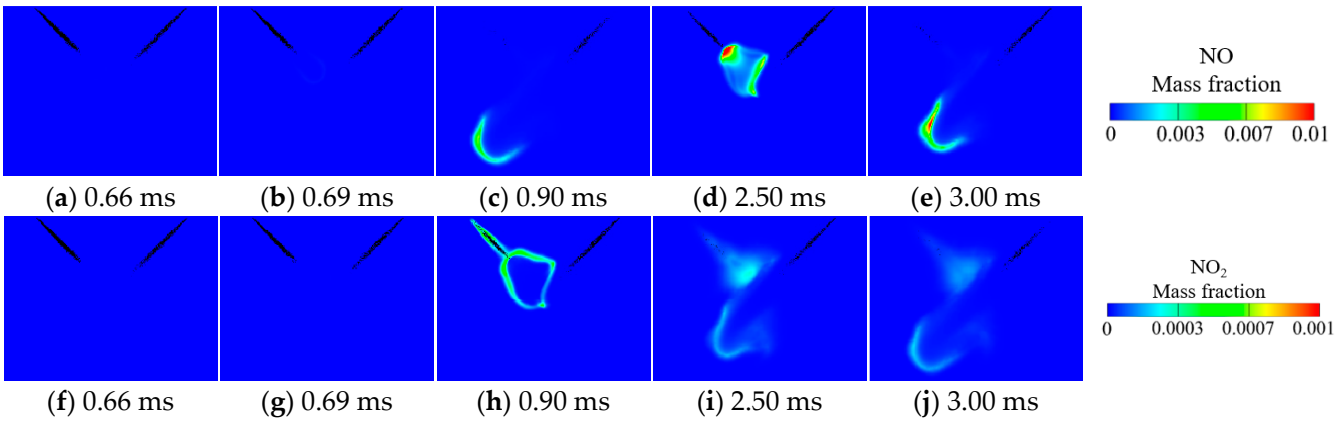

Figure 10. The NO and NO_2 distributions at θ = 90°.

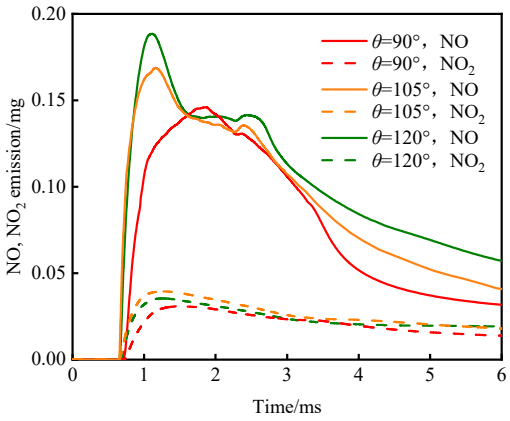

Figure 11. NO and NO_2 emissions with different θ.

3.2. Effect of NH_3 Injection Pressure on Ignition and Combustion Process

Fuel injection pressure is critical in determining atomization quality and penetration distance, which strongly influence combustion and emissions characteristics. In this study, the DME injection pressure is fixed at 75 MPa, while the liquid ammonia injection pressure P_{NH_3} varies at 60 MPa, 75 MPa, and 90 MPa. The maximum temperature at each P_{NH_3} is presented in Figure 12a. The highest maximum temperature is observed for P_{NH_3} = 60 MPa, followed by 75 MPa and 90 MPa. Higher P_{NH_3} enhances atomization and accelerates droplet evaporation, intensifying the cooling effect on the DME flame. During injection, increased P_{NH_3} shortens the ammonia injection duration, facilitating an earlier transition to the combustion phase. As shown in Figure 12b, the liquid ammonia combustion efficiency decreases slightly from 93.08% to 91.21% as P_{NH_3} increases from 60 MPa to 90 MPa, representing a reduction of approximately 2%.

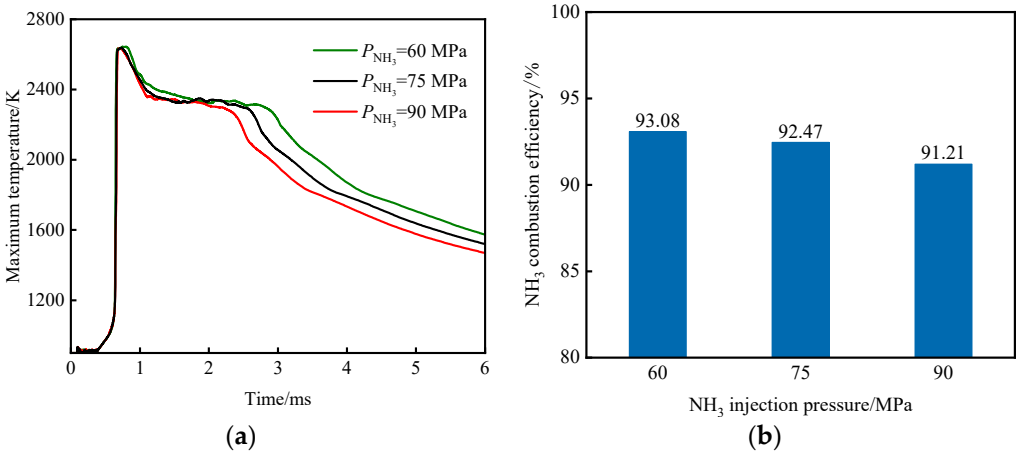

Figure 12. Thermal conditions for different P_{NH_3}. (**a**) Maximum temperature, (**b**) Ammonia combustion efficiency.

The temperature distributions at the ignition moment for varying P_{NH_3} are shown in Figure 13, indicating that higher P_{NH_3} increases the penetration velocity of the ammonia spray. This results in a larger contact area during its interaction with the DME flame, leading to greater heat absorption from DME combustion via ammonia evaporation. As P_{NH_3} increases, the high-temperature region at the DME spray head shrinks, and the temperature decreases slightly due to increased heat absorption. The velocity contours for varying ammonia injection pressure are presented in Figure 14, showing that the vortex at the head of the liquid ammonia spray becomes more pronounced with higher P_{NH_3}, enhancing air entrainment and fuel mixing.

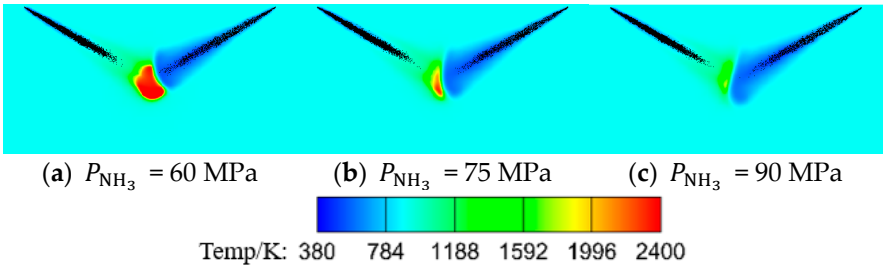

Figure 13. Temperature contours at ignition moment with different P_{NH_3}.

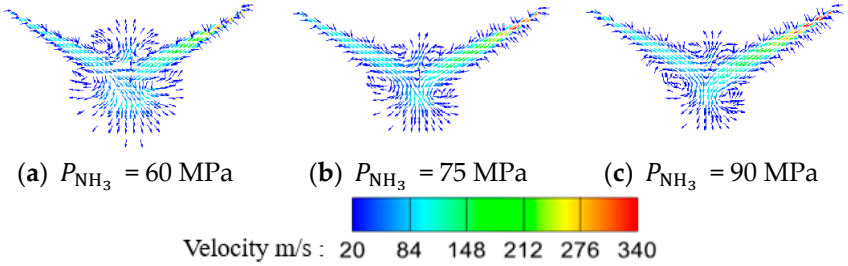

Figure 14. Velocity contours at ignition moment with different P_{NH_3}.

The distributions of temperature, OH, NH_3, DME, NH_2, NO, and NO_2 under $P_{NH_3} = 60$ MPa are presented in Figures 15 and 16, while those at $P_{NH_3} = 90$ MPa are depicted in Figures 17 and 18 for comparative analysis. At 0.66 ms, DME combustion begins under $P_{NH_3} = 60$ MPa, accompanied by OH radical formation. In contrast, at $P_{NH_3} = 90$ MPa, no significant high-temperature regions or OH radicals are observed. By 0.70 ms, the higher injection pressure splits the DME flame into two high-temperature regions, Meanwhile, increased ammonia evaporation and cooling effects further shrink the flame, reducing its size. At 0.90 ms, with $P_{NH_3} = 60$ MPa, the DME flame front fully envelops the ammonia spray head. However, the lower injection pressure reduces atomization efficiency, leading to a noticeable accumulation of liquid ammonia particles near the spray head. Furthermore, the DME concentration is lower at $P_{NH_3} = 90$ MPa during the same period. During the early combustion stage, DME is less influenced by the ammonia spray, allowing it to burn more rapidly. At 2.50 ms, the flame temperature is higher under $P_{NH_3} = 60$ MPa because the lower injection pressure extends the ammonia injection duration, allowing the influx of cold ammonia to lower internal spray temperatures. By 3.00 ms, the mass fraction of unburned ammonia at $P_{NH_3} = 60$ MPa remains similar to its value at 2.50 ms. The high-temperature region at $P_{NH_3} = 60$ MPa is larger and more uniformly distributed, providing sufficient heat for ammonia combustion. The increased presence of OH radicals near the ammonia spray head indicates more vigorous combustion, suggesting that lower P_{NH_3} can moderately improve ammonia combustion efficiency. Figure 19 shows the NO and NO_2 distribution for the whole combustion process under different ammonia injection pressure, as P_{NH_3} increases from 60 MPa to 90 MPa, the peak NO concentration rises significantly. This trend is attributed to enhanced mixing between ammonia and DME sprays at higher injection pressures, which enhances combustion efficiency and raises temperatures, promoting both thermal and fuel NO formation. At $P_{NH_3} = 90$ MPa, a high NO concentration region is observed near the DME spray head at approximately 0.9 ms. This corresponds to the reaction of NH_2 radicals with oxygen at elevated temperatures, forming NO. After peaking, NO concentration gradually decreases over time. During the ammonia combustion phase, temperatures decrease, enabling NO reduction to N_2 in the cooler post-flame region. While peak NO emissions vary, final NO emissions are nearly identical across all P_{NH_3} conditions. NO_2 production remains less sensitive to ammonia injection pressure.

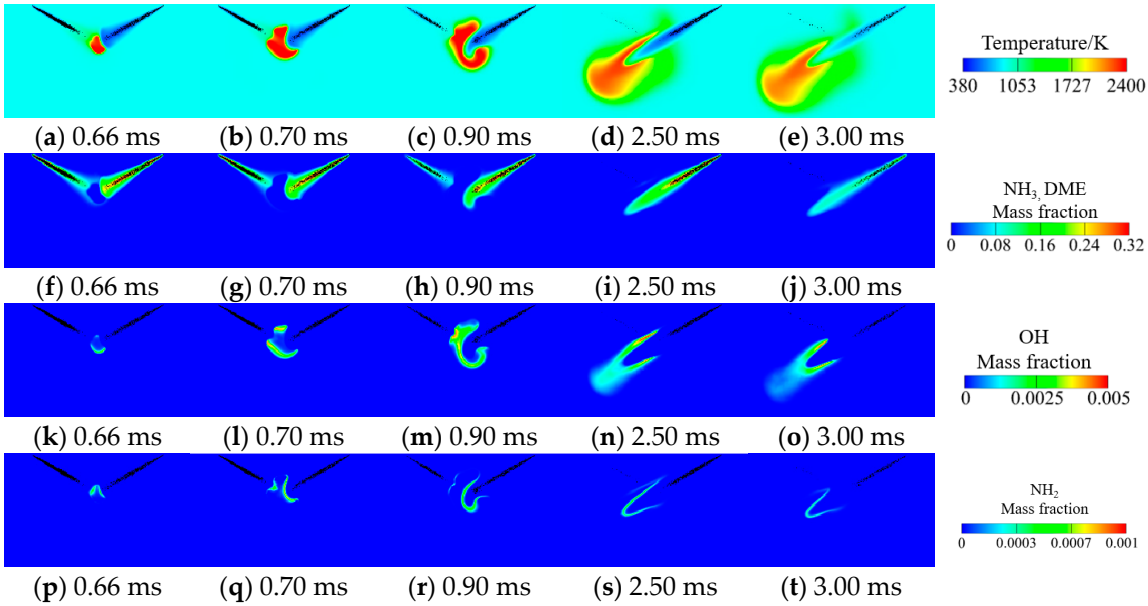

Figure 15. The temperature, OH, NH_3, DME, and NH_2 distributions at P_{NH_3} = 60 MPa.

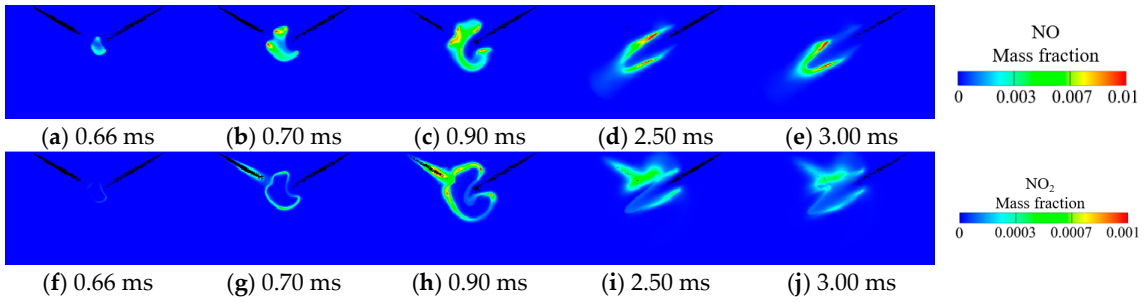

Figure 16. The NO and NO_2 distributions at P_{NH_3} = 60 MPa.

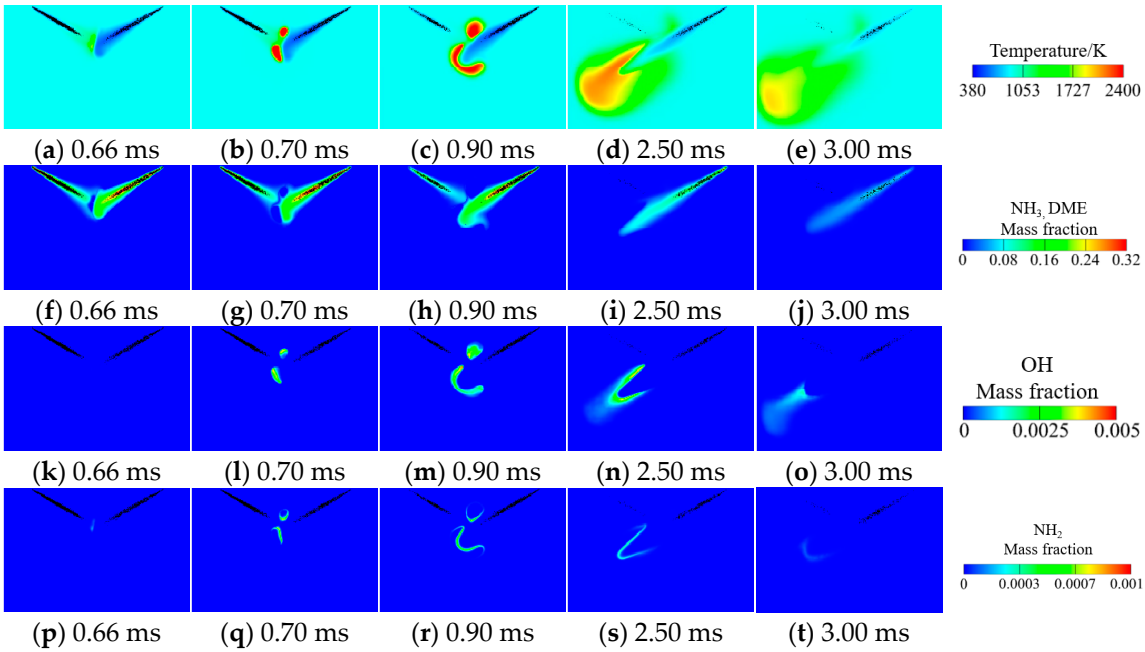

Figure 17. The temperature, OH, NH_3, DME, and NH_2 distributions at P_{NH_3} = 90 MPa.

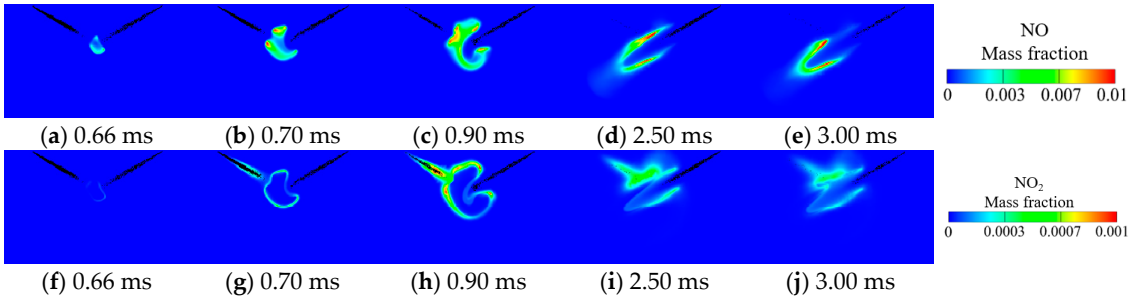

Figure 18. The NO and NO_2 distributions at P_{NH_3} = 90 MPa.

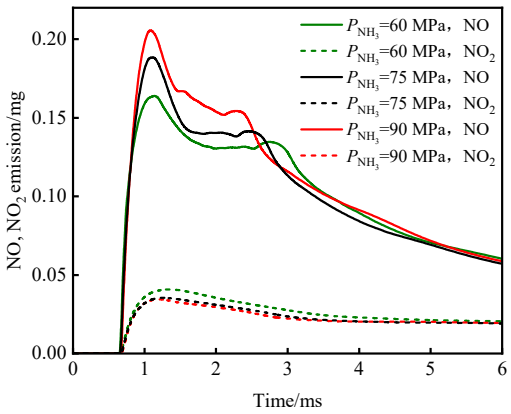

Figure 19. NO and NO_2 emissions with different P_{NH_3}.

3.3. Effect of Ambient Pressure on Ignition and Combustion Process

In addition to injector angles and injection pressures, ambient conditions play a critical role in combustion processes, enabling optimization of chamber operating conditions. This study investigates the effects of ambient pressures ranging from 2.8 MPa to 5.8 MPa on combustion.

The maximum temperature and NH_3 combustion efficiency at varying ambient pressures are shown in Figure 20. At P_a = 2.8 MPa, ignition fails due to insufficient mixing and the pronounced cooling effects of ammonia evaporation, which inhibit temperature rise. Successful ignition occurs at P_a > 2.8 MPa. As P_a increases, the ignition delay time decreases. Higher ambient pressure improves heat exchange between the DME spray and surrounding air, enhancing atomization and evaporation, and thereby accelerating ignition. Additionally, higher P_a increases local oxygen concentration and air density, promoting more effective DME–oxygen mixing and faster combustion. Higher ambient pressures produce higher peak maximum temperatures. However, the post-combustion cooling rate increases with P_a due to the greater heat absorption from ammonia vaporization. Ammonia combustion efficiency peaks at P_a = 3.8 MPa with 92.47%, decreases to 86.87% at P_a = 4.8 MPa, and further declines to 70.59% at P_a = 5.8 MPa. Figure 21 presents temperature contours at ignition moments for varying ambient pressures. At low ambient pressure (P_a = 2.8 MPa), no high-temperature zone forms, and the DME spray contacts the cold liquid ammonia spray before ignition. Significant ammonia evaporation and heat absorption reduce the temperature at the DME spray head, suppressing ignition. At P_a = 3.8 MPa, a localized high-temperature region forms at the interface between the DME and ammonia sprays, facilitating successful ignition. This interaction is key to achieving high ammonia combustion efficiency. At P_a = 4.8 MPa and 5.8 MPa, higher ambient pressures restrict the axial propagation of the DME spray, causing ignition to occur closer to the nozzle. At P_a = 5.8 MPa, the high-temperature region is even closer to the nozzle. Reduced interaction

between the DME and ammonia sprays at higher pressures further decreases ammonia combustion efficiency.

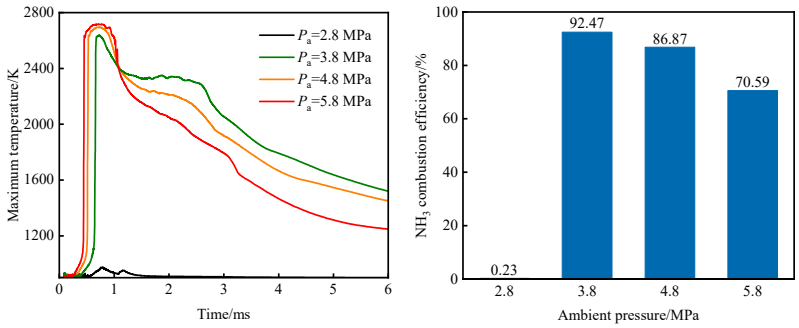

Figure 20. Thermal conditions for different ambient pressure. (**a**) Maximum temperature, (**b**) Ammonia combustion efficiency.

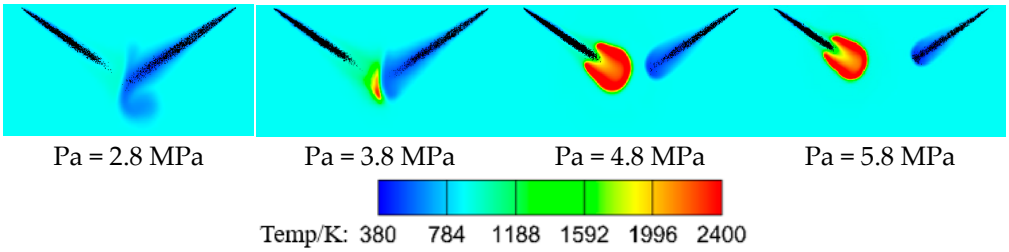

Figure 21. Temperature at ignition moment at different Pa.

Figures 22–25 compare the distributions of temperature, OH, NH_3, DME, NH_2, NO, and NO_2 for P_a = 3.8 MPa and P_a = 5.8 MPa. At P_a = 3.8 MPa, DME ignites and interacts with the liquid ammonia spray at 0.66 ms. At P_a = 5.8 MPa, higher ambient pressure causes DME to ignite closer to the nozzle. Due to reduced influence from the liquid ammonia spray, the flame region at P_a = 5.8 MPa is larger than that at P_a = 3.8 MPa at 0.90 ms. However, the flame front does not fully envelop the liquid ammonia spray, limiting interaction between the cold ammonia spray and the high-temperature flame. At P_a = 5.8 MPa, early-stage DME combustion is more complete, leaving almost no unburned DME by 2.50 ms. Consequently, the flame temperature is lower than at P_a = 3.8 MPa, primarily due to incomplete early-stage combustion of liquid ammonia, which reduces the overall combustion rate and results in inefficient combustion. By 3.00 ms, OH radicals nearly disappear at P_a = 5.8 MPa, with no significant high-temperature regions remaining. A higher fraction of unburned ammonia is observed at P_a = 5.8 MPa compared to P_a = 3.8 MPa, indicating reduced combustion efficiency at higher pressures. Insufficient flame–ammonia interaction limits the conversion of ammonia into reactive intermediates, such as NH_2. At both pressures, NO formation begins shortly after DME ignition. At P_a = 5.8 MPa, NO forms before the interaction, primarily through thermal NO formation from atmospheric nitrogen. At P_a = 3.8 MPa, NO is generated alongside and propagates with the liquid ammonia spray, resulting in high NO concentrations at the ammonia spray front. Further downstream, NO oxidizes to NO_2 as the flame maintains temperatures conducive to oxidation reactions. At P_a = 5.8 MPa, the absence of stable ammonia combustion reduces NO formation at the ammonia spray front.

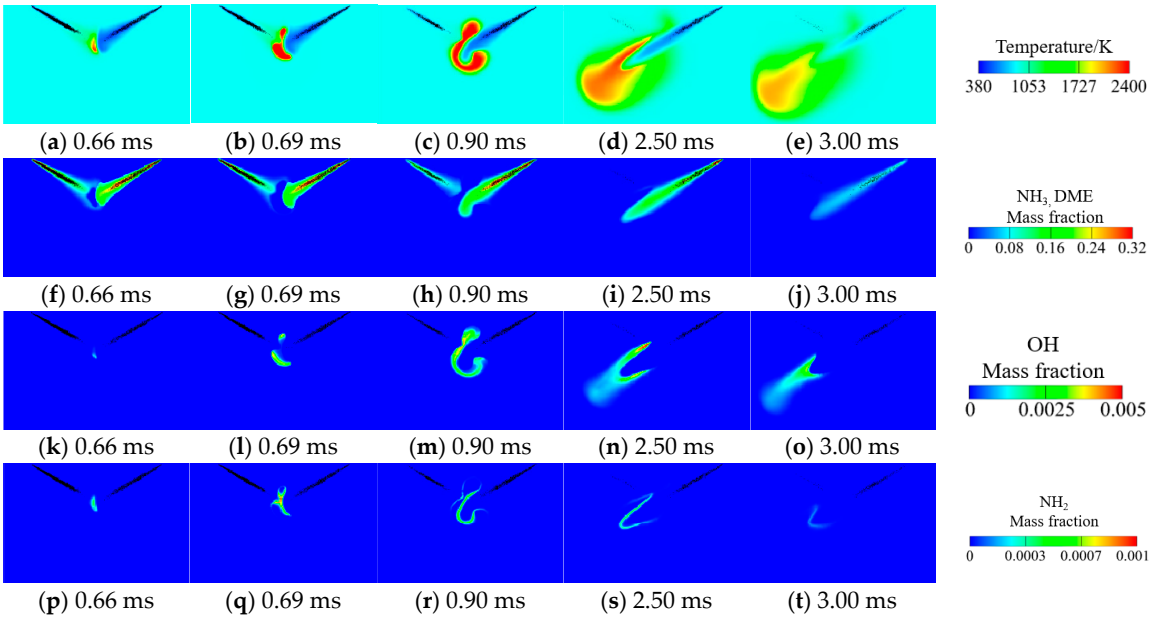

Figure 22. The temperature, OH, NH_3, DME, and NH_2 distributions at P_a = 3.8 MPa.

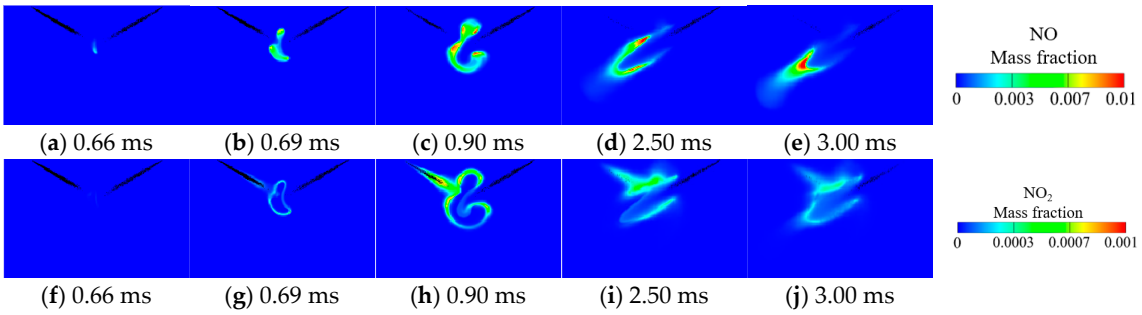

Figure 23. The NO and NO_2 distributions at P_a = 3.8 MPa.

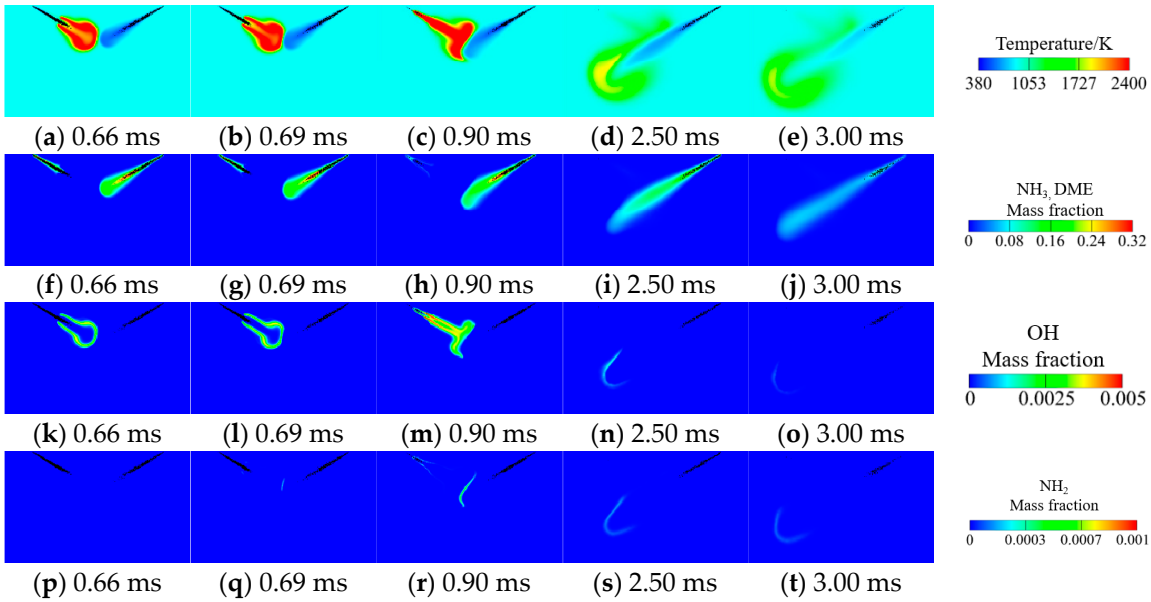

Figure 24. The temperature, OH, NH_3, DME, and NH_2 distributions at P_a = 5.8 MPa.

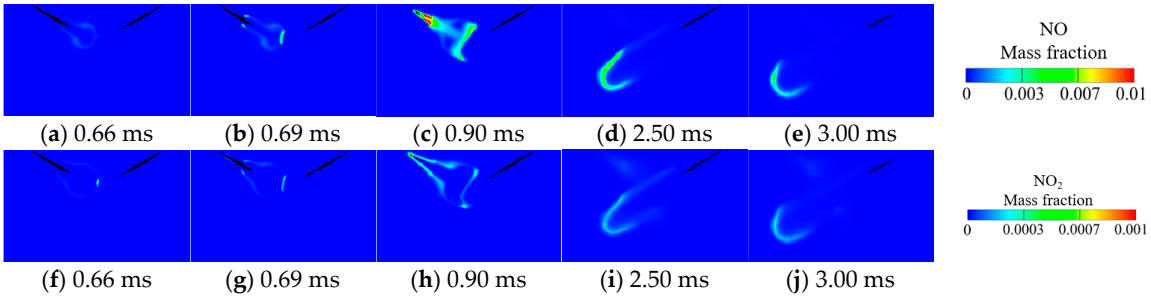

(**a**) 0.66 ms (**b**) 0.69 ms (**c**) 0.90 ms (**d**) 2.50 ms (**e**) 3.00 ms

(**f**) 0.66 ms (**g**) 0.69 ms (**h**) 0.90 ms (**i**) 2.50 ms (**j**) 3.00 ms

Figure 25. The NO and NO_2 distributions at P_a = 5.8 MPa.

Figure 26 illustrates variations in NO and NO_2 under different ambient pressures, with NO formation starting at 0.46 ms across all pressures, preceding liquid ammonia combustion. The highest NO formation rate is observed at P_a = 3.8 MPa, where the peak NO emission is approximately 54.35% higher than that at P_a = 5.8 MPa. Higher ambient pressures consistently result in lower NO emissions. At the post-combustion stage, NO emissions at P_a = 3.8 MPa remain 153% higher than that at P_a = 5.8 MPa. NO reacts with oxygen to form NO_2, first appearing after 0.80 ms. This delay occurs because NO oxidation to NO_2 is temperature-dependent. At lower pressures, NO_2 peaks are broader, indicating more prolonged oxidation reactions. Conversely, at higher pressures (P_a = 5.8 MPa), NO_2 formation occurs over a shorter duration due to reduced temperatures limiting reaction rates. When the liquid ammonia spray ignites, NO and NO_2 form at its head with accelerated generation rates. Increasing ambient pressure significantly reduces NO and NO_2 production, leading to lower emissions but reduced combustion efficiency. Among the three factors investigated, injection angle and ambient pressure exert the greatest influence on liquid ammonia combustion efficiency and emissions compared to injection pressure. Figure 27 presents a comprehensive analysis of the effects of injection angle (θ) and ambient pressure (P_a) on liquid ammonia combustion efficiency and NO emissions. The dashed and solid lines in Figure 27a represent 80% and 90% combustion efficiency contours, respectively. Smaller injection angles (θ = 90°, 105°) provide a larger combustible range but lower combustion efficiency. Increasing the angle to 120°, along with moderate ambient pressure, achieves combustion efficiencies exceeding 90%. When the injection angle exceeds 120°, ammonia combustion efficiency decreases, with a higher risk of misfire. Figure 27b evaluates NO emissions under the same operating conditions. It reveals a strong correlation between higher ammonia combustion efficiency and elevated NO emissions. The peak NO emissions of over 0.05 mg occur within the region where the combustion efficiency exceeds 90%, emphasizing the trade-off between combustion performance and pollutant formation. Modes with lower combustion efficiency, particularly those susceptible to misfire, exhibit significantly lower NO emissions. Four of the 20 modes achieve efficiencies exceeding 80%, identified as Modes 1–4, with specific combinations detailed in Table 6. Figure 28 compares the ammonia combustion efficiency, and the NO and NO_2 emissions across modes. Mode 2 produces the lowest NO and NO_2 emissions but also exhibits the lowest combustion efficiency. Mode 3 achieves the highest combustion efficiency, exceeding 90%, but also produces the highest NO and NO_2 emissions. Modes 1 and 4 achieve higher efficiencies than Mode 2 but are associated with increased emissions. In conclusion, Mode 3 offers the best balance between minimizing unburned ammonia and achieving high combustion efficiency. However, its practical application requires mitigating the environmental impact of NO and NO_2 emissions, necessitating the integration of emissions control systems such as selective catalytic reduction.

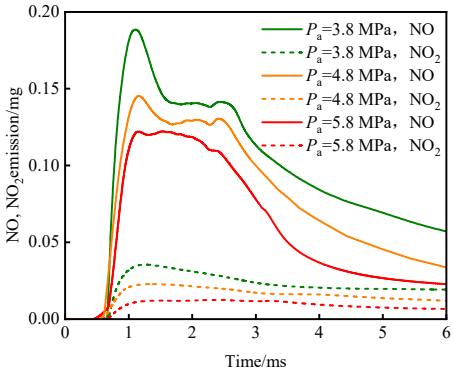

Figure 26. NO and NO_2 emissions with different Pa.

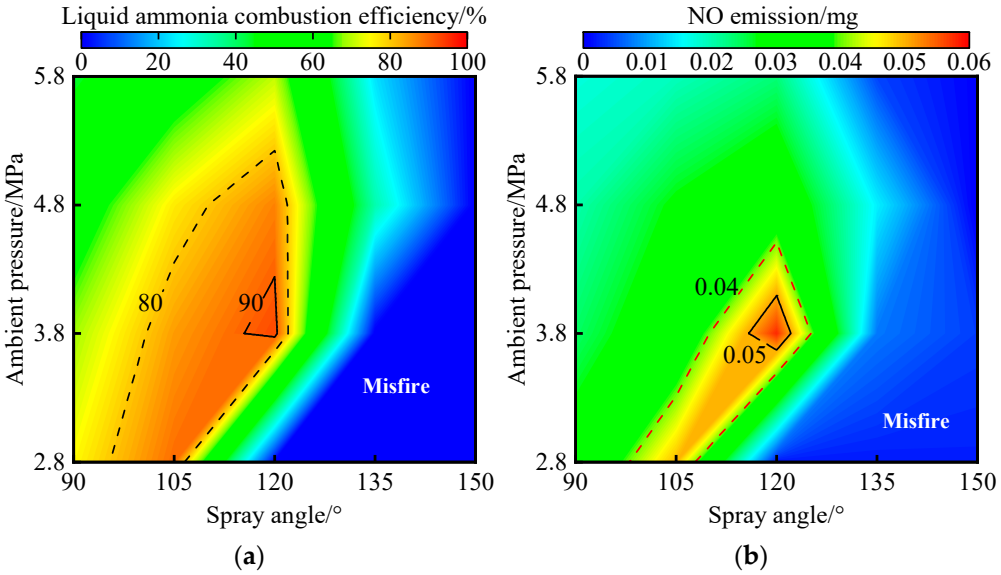

Figure 27. Combustion and emissions with different θ and P_a. (**a**) The liquid ammonia combustion efficiency, (**b**) NO emissions.

Table 6. Specifications for ammonia combustion efficiency of over 80%.

Modes	Angle/°	Ambient Pressure/MPa
Mode 1	105°	2.8
Mode 2	105°	3.8
Mode 3	120°	3.8
Mode 4	120°	4.8

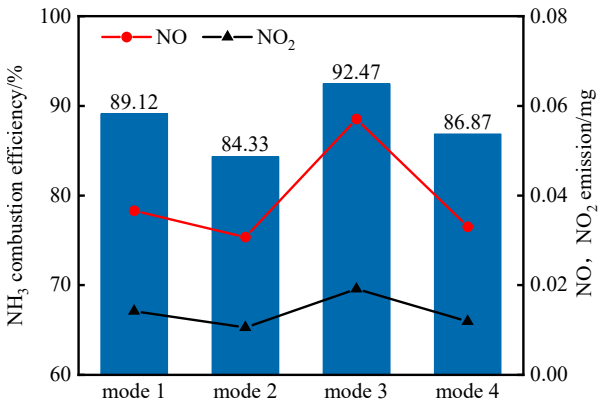

Figure 28. Comparison of combustion efficiency and emissions of modes 1–4.

4. Conclusions

This study conducted a numerical investigation of NH_3 spray ignition by dimethyl ether spray in a constant-volume chamber. The effects of injection angles (90° to 150°), NH_3 injection pressures (60 to 90 MPa), and ambient pressures (2.8 to 5.8 MPa) on ignition and emissions were investigated. The main conclusions are summarized below.

Increasing the injection angle improves mixing between liquid ammonia and dimethyl ether sprays, promoting more uniform combustion. However, excessively large injection angles lead to incomplete combustion or even misfire. Larger injection angles under combustible conditions produce higher combustion efficiency and increased NO emissions, with one specific 120° condition reaching over 90% liquid ammonia combustion efficiency.

Higher liquid ammonia injection pressure improves atomization and evaporation, advancing the interaction between ammonia and dimethyl ether sprays. However, excessively high injection pressure intensifies the cooling effect, reducing ammonia combustion efficiency. Elevated liquid ammonia injection pressure also divides the high-temperature region of dimethyl ether combustion, resulting in a higher NO formation peak. NO and NO_2 concentrations show minimal variations across different injection pressures.

The evaporation of liquid ammonia suppresses dimethyl ether ignition at low ambient pressures. As ambient pressure increases, liquid ammonia ignition becomes feasible; however, dimethyl ether combustion occurs earlier and closer to the nozzle. Liquid ammonia combustion efficiency decreases at higher ambient pressures. Both NO and NO_2 production decrease as ambient pressure increases.

Based on these findings, liquid ammonia injection pressure has a smaller influence on ignition process than injection angle and ambient pressure. A spray angle of 120°, liquid ammonia injection pressure of 75 MPa, and ambient pressure of 3.8 MPa are recommended to achieve high combustion efficiency, while the NO_x emissions require treatment in the exhaust gas.

Author Contributions: Conceptualization, L.D. and Q.W.; methodology, Y.L. and Q.W.; software, Y.L. and J.L.; validation, Y.L. and O.Y.; formal analysis, J.L. and O.Y.; investigation, Y.L.; data curation, Y.L.; writing—original draft preparation, Y.L.; writing—review and editing, N.J.S. and L.D.; supervision, N.J.S.; funding acquisition, L.D. All authors have read and agreed to the published version of the manuscript.

Funding: This research was funded by the National Natural Science Foundation of China (grant No. 52206149).

Institutional Review Board Statement: Not applicable.

Informed Consent Statement: Not applicable.

Data Availability Statement: The data that support the findings of this study are available from the corresponding author upon reasonable request.

Conflicts of Interest: The authors declare no conflicts of interest.

References

1. Wu, P.; Xuan, T.; He, Z.; Shao, Z.; Wang, Q.; Payri, R. A comparative study on combustion characteristics of PPC and RCCI combustion modes in an optical engine with renewable fuels. *Fuel* **2025**, *381*, 133361. [CrossRef]
2. Zhong, W.; Dai, L.; He, Z.; Wang, Q. Numerical study on the combustion characteristics of premixed ammonia flames with methanol/ethanol/n-butanol addition. *Fuel* **2025**, *381*, 133527. [CrossRef]
3. Song, Y.; Zhu, H.; Shen, Y.; Yan, Z.; Feng, S. Zero-carbon tunnel: Concept, methodology and application in the built environment. *J. Clean. Prod.* **2024**, *479*, 144031. [CrossRef]
4. Qi, Y.; Liu, W.; Liu, S.; Wang, W.; Peng, Y.; Wang, Z. A review on ammonia-hydrogen fueled internal combustion engines. *eTransportation* **2023**, *18*, 100288. [CrossRef]

5. Xing, H.; Stuart, C.; Spence, S.; Chen, H. Alternative fuel options for low carbon maritime transportation: Pathways to 2050. *J. Clean. Prod.* **2021**, *297*, 126651. [CrossRef]
6. Zhang, J.; Chen, D.; Li, X.; Li, J.; Huang, H.; Kobayashi, N. Large eddy simulation of ammonia-diesel dual fuel spray combustion: Effects of ambient condition on ignition characteristics. *Chem. Eng. J.* **2024**, *501*, 157698. [CrossRef]
7. Qin, W.; Shi, J.; Cheng, Q. Numerical study on diesel ignited methane-hydrogen tri-fuel RCCI combustion. *Fuel* **2025**, *381*, 133605. [CrossRef]
8. Wang, G.; Chen, C.; Beshiwork, B.A.; Lin, B. Developing a low-carbon hybrid of ammonia fuel cell and internal combustion engine for carbon neutrality. *Appl. Energy Combust. Sci.* **2023**, *16*, 100214. [CrossRef]
9. Li, G.; Wang, J.; Wang, H.; Tang, Q.; Liu, H.; Yao, M. Experimental investigation on the regulation of methane addition for multi-stage combustion of lean ammonia/air mixtures using jet ignition. *Energy* **2024**, *313*, 133905. [CrossRef]
10. Sonker, M.; Tiwary, S.K.; Shreyash, N.; Bajpai, S.; Ray, M.; Kar, S.K.; Balathanigaimani, M.S. Ammonia as an alternative fuel for vehicular applications: Paving the way for adsorbed ammonia and direct ammonia fuel cells. *J. Clean. Prod.* **2022**, *376*, 133960. [CrossRef]
11. Zhao, H. The role of green ammonia in meeting challenges towards a sustainable development in China. *Energy* **2024**, *310*, 133283. [CrossRef]
12. Takizawa, K.; Takahashi, A.; Tokuhashi, K.; Kondo, S.; Sekiya, A. Burning velocity measurements of nitrogen-containing compounds. *J. Hazard. Mater.* **2008**, *155*, 144–152. [CrossRef] [PubMed]
13. Kobayashi, H.; Hayakawa, A.; Somarathne, K.D.K.A.; Okafor, E.C. Science and technology of ammonia combustion. *Proc. Combust. Inst.* **2019**, *37*, 109–133. [CrossRef]
14. Xiao, H.; Li, H. Experimental and kinetic modeling study of the laminar burning velocity of NH3/DME/air premixed flames. *Combust. Flame* **2022**, *245*, 112372. [CrossRef]
15. Wang, X.; Li, T.; Zhou, X.; Huang, S.; Chen, R.; Yi, P.; Lv, Y.; Wang, Y.; Rao, H.; Liu, Y.; et al. Reductions in GHG and unburned ammonia of the pilot diesel-ignited ammonia engines by diesel injection strategies. *Appl. Therm. Eng.* **2025**, *260*, 124967. [CrossRef]
16. Jayabal, R.; Lionus Leo, G.M.; Chrispin Das, M.; Sekar, S.; Arivazhagan, S. Impact of ammonia energy fraction on improving thermal efficiency and emissions of ammonia/biodiesel in dual fuel diesel engine. *Process Saf. Environ. Prot.* **2024**, *188*, 1398–1410. [CrossRef]
17. D'Antuono, G.; Galloni, E.; Lanni, D.; Contino, F.; Brequigny, P.; Mounaïm-Rousselle, C. Assessment of combustion development and pollutant emissions of a spark ignition engine fueled by ammonia and ammonia-hydrogen blends. *Int. J. Hydrogen Energy* **2024**, *85*, 191–199. [CrossRef]
18. Zhang, X.; Meng, X.; Zhu, W.; Long, W.; Bi, M. Experimental and simulated study of ammonia blending with DME steam reformed and cracked gases under lean-burn condition. *Int. J. Hydrogen Energy* **2024**, *94*, 464–473. [CrossRef]
19. Ruiz-Gutiérrez, A.; Rebollo, P.; Alzueta, M.U. Combustion of NH3/DME and NH3/DME/NO mixtures. *Fuel* **2025**, *381*, 133253. [CrossRef]
20. Liu, L.; Wu, Y.; Wang, Y.; Wu, J.; Fu, S. Exploration of environmentally friendly marine power technology-ammonia/diesel stratified injection. *J. Clean. Prod.* **2022**, *380*, 135014. [CrossRef]
21. Elumalai, R.; Ravi, K. Strategy to reduce carbon emissions by adopting ammonia–Algal biodiesel in RCCI engine and optimize the fuel concoction using RSM methodology. *Int. J. Hydrogen Energy* **2022**, *47*, 39701–39718. [CrossRef]
22. Füzesi, D.; Wang, S.; Józsa, V.; Chong, C.T. Ammonia-methane combustion in a swirl burner: Experimental analysis and numerical modeling with Flamelet Generated Manifold model. *Fuel* **2023**, *341*, 127403. [CrossRef]
23. Xu, L.; Xu, S.; Bai, X.-S.; Repo, J.A.; Hautala, S.; Hyvönen, J. Performance and emission characteristics of an ammonia/diesel dual-fuel marine engine. *Renew. Sustain. Energy Rev.* **2023**, *185*, 113631. [CrossRef]
24. Yousefi, A.; Guo, H.; Dev, S.; Liko, B.; Lafrance, S. Effects of ammonia energy fraction and diesel injection timing on combustion and emissions of an ammonia/diesel dual-fuel engine. *Fuel* **2022**, *314*, 122723. [CrossRef]
25. Li, T.; Zhou, X.; Wang, N.; Wang, X.; Chen, R.; Li, S.; Yi, P. A comparison between low- and high-pressure injection dual-fuel modes of diesel-pilot-ignition ammonia combustion engines. *J. Energy Inst.* **2022**, *102*, 362–373. [CrossRef]
26. Liu, X.; Wang, Q.; Zhong, W.; Jiang, P.; Xu, M.; Guo, B. An optical investigation of the effects of diesel injection pressure and intake air temperature in an ammonia-diesel dual-fuel engine under low-load conditions. *Appl. Therm. Eng.* **2025**, *261*, 125174. [CrossRef]
27. Zhang, Z.; Long, W.; Dong, P.; Tian, H.; Tian, J.; Li, B.; Wang, Y. Performance characteristics of a two-stroke low speed engine applying ammonia/diesel dual direct injection strategy. *Fuel* **2023**, *332*, 126086. [CrossRef]
28. Shi, C.; Zhang, Z.; Wang, H.; Wang, J.; Cheng, T.; Zhang, L. Parametric analysis and optimization of the combustion process and pollutant performance for ammonia-diesel dual-fuel engines. *Energy* **2024**, *296*, 131171. [CrossRef]
29. Yu, C.; Guo, L.; Sun, W.; Zhang, H.; Cheng, P.; Yan, Y.; Zhu, G.; Jiang, M.; Guo, Y.; Yue, F. Experimental and chemical kinetic study on effects of H2-DME fusion addition on laminar premixed flame speed and flame instability for ammonia composite combustion. *Energy* **2024**, *310*, 133175. [CrossRef]

30. Inayat, A.; Ghenai, C.; Naqvi, M.; Ammar, M.; Ayoub, M.; Hussin, M.N.B. Parametric Study for Production of Dimethyl Ether (DME) As a Fuel from Palm Wastes. *Energy Procedia* **2017**, *105*, 1242–1249. [CrossRef]
31. Im-orb, K.; Arpornwichanop, A. Comparative techno-economic assessment of bio-methanol and bio-DME production from oil palm residue. *Energy Convers. Manag.* **2022**, *258*, 115511. [CrossRef]
32. Sun, C.; Liu, Y.; Qiao, X.; Ju, D.; Tang, Q.; Fang, X.; Zhou, F. Experimental study of effects of exhaust gas recirculation on combustion, performance, and emissions of DME-biodiesel fueled engine. *Energy* **2020**, *197*, 117233. [CrossRef]
33. Gross, C.W.; Kong, S.-C. Performance characteristics of a compression-ignition engine using direct-injection ammonia–DME mixtures. *Fuel* **2013**, *103*, 1069–1079. [CrossRef]
34. Ryu, K.; Zacharakis-Jutz, G.E.; Kong, S.-C. Performance characteristics of compression-ignition engine using high concentration of ammonia mixed with dimethyl ether. *Appl. Energy* **2014**, *113*, 488–499. [CrossRef]
35. Zhu, J.; Zhou, D.; Yang, W.; Qian, Y.; Mao, Y.; Lu, X. Investigation on the potential of using carbon-free ammonia in large two-stroke marine engines by dual-fuel combustion strategy. *Energy* **2023**, *263*, 125748. [CrossRef]
36. Beale, J.C.; Reitz, R. Modeling Spray Atomization with the Kelvin-Helmholtz/Rayleigh-Taylor Hybrid Model. *At. Sprays* **1999**, *9*, 623–650. [CrossRef]
37. Krishnamoorthy, V.; Dhanasekaran, R.; Rana, D.; Saravanan, S.; Rajesh Kumar, B. A comparative assessment of ternary blends of three bio-alcohols with waste cooking oil and diesel for optimum emissions and performance in a CI engine using response surface methodology. *Energy Convers. Manag.* **2018**, *156*, 337–357. [CrossRef]
38. HAN, Z.; REITZ, R.D. Turbulence Modeling of Internal Combustion Engines Using RNG κ-ε Models. *Combust. Sci. Technol.* **1995**, *106*, 267–295. [CrossRef]
39. O'Rourke, P.J.; Amsden, A.A. A Spray/Wall Interaction Submodel for the KIVA-3 Wall Film Model. *SAE Trans.* **2000**, *109*, 281–298.
40. Schmidt, D.P.; Rutland, C.J. A New Droplet Collision Algorithm. *J. Comput. Phys.* **2000**, *164*, 62–80. [CrossRef]
41. Hiroyasu, H.; Kadota, T. *Models for Combustion and Formation of Nitric Oxide and Soot in Direct Injection Diesel Engines*; SAE Paper 760129; Society of Automotive Engineers, Inc.: Warrendale, PA, USA, 1976.
42. Zhang, J.; Chen, D.; Lai, S.; Li, J.; Huang, H.; Kobayashi, N. Numerical simulation and spray model development of liquid ammonia injection under diesel-engine conditions. *Energy* **2024**, *294*, 130833. [CrossRef]
43. Cung, K. Spray and Combustion Characteristics of Dimethyl Ether Under Various Ambient Conditions: An Experimental and Modeling Study. Master's Thesis, Michigan Technological University, Houghton, MI, USA, 2015. [CrossRef]
44. Cung, K.; Moiz, A.; Johnson, J.; Lee, S.-Y.; Kweon, C.-B.; Montanaro, A. Spray–combustion interaction mechanism of multiple-injection under diesel engine conditions. *Proc. Combust. Inst.* **2015**, *35*, 3061–3068. [CrossRef]
45. Huo, J.; Zhao, T.; Lin, H.; Li, J.; Zhang, W.; Huang, Z.; Han, D. Study on lean combustion of ammonia-hydrogen mixtures in a pre-chamber engine. *Fuel* **2024**, *361*, 130773. [CrossRef]

Disclaimer/Publisher's Note: The statements, opinions and data contained in all publications are solely those of the individual author(s) and contributor(s) and not of MDPI and/or the editor(s). MDPI and/or the editor(s) disclaim responsibility for any injury to people or property resulting from any ideas, methods, instructions or products referred to in the content.

https://dspace.org/

Numerical study on the combustion and emissions characteristics of liquid ammonia spray ignited by dimethyl ether spray

Leng, Yupeng; Dai, Liming; Wang, Qian; Lu, Jiayu; Yu, Ouqing ...

2024-12-31
MDPI
https://doi.org/10.3390/fire8010014
Leng Y, Dai L, Wang Q, et al., (2024) Numerical study on the combustion and emissions characteristics of liquid ammonia spray ignited by dimethyl ether spray. Fire, Volume 8, Issue 1, December 2024, Article number 14

Downloaded from a DSpace repository. https://dspace.org/